

Two-dimensional Dirac nodal-line semimetal against strong spin-orbit coupling in real materials

Xingxia Cui^{1†}, Yafei Li^{1†}, Deping Guo^{2†}, Pengjie Guo^{2,3,4†}, Cancan Lou¹, Guangqiang Mei¹, Chen Lin⁵, Shijing Tan⁵, Zhengxin Liu², Kai Liu², Zhongyi Lu², Hrvoje Petek⁶, Limin Cao¹, Wei Ji^{2*} & Min Feng^{1,7*}

¹School of Physics and Technology and Key Laboratory of Artificial Micro- and Nano-Structures of Ministry of Education, Wuhan University, Wuhan 430072, China

²Beijing Key Laboratory of Optoelectronic Functional Materials & Micro-Nano Devices, Department of Physics, Renmin University of China, Beijing 100872, China

³Songshan Lake Materials Laboratory, Dongguan, Guangdong 523808, China

⁴Beijing National Laboratory for Condensed Matter Physics, and Institute of Physics, Chinese Academy of Sciences, Beijing 100190, China

⁵Hefei National Laboratory for Physical Sciences at the Microscale, University of Science and Technology of China, Hefei, Anhui 230026, China

⁶Department of Physics and Astronomy and Pittsburgh Quantum Institute, University of Pittsburgh, Pittsburgh, PA 15260, USA

⁷Institute for Advanced Studies, Wuhan University, Wuhan 430072, China

†These authors contributed equally to this work.

*Corresponding author. Email: wji@ruc.edu.cn (W.J.); fengmin@whu.edu.cn (M.F.)

Abstract: Symmetry is one of the conceptual pillars underlying fundamental understanding of electronic band structures of materials¹. Unique symmetries have boosts continuous discoveries of Dirac materials with intriguing electronic phases in the past decade²⁻⁶. A long-standing challenge in the community lies in searching for robust Dirac nodal line semimetals (DNLSs) in two-dimensional (2D) systems⁷⁻¹⁰, where the low-energy fermionic excitations along the four-fold degenerate Dirac nodal line (DNL) would essentially dominate the electrical properties of the 2D materials.

However, such four-fold degenerate lines are usually vulnerable to spin-orbit coupling (SOC)⁷⁻¹¹. A real 2D DNLS material, that shows robustness to SOC, is yet to be experimentally discovered or proved. Here, by combining molecular beam epitaxy growth on black phosphorus substrates (BP), scanning tunneling microscopy (STM) characterization, density functional theory (DFT) calculations and space group theory analysis, we reveal a solely symmetry dictated SOC-robust DNL in real 2D crystalline structures. A tri-atomic layers bismuth (3-ALs Bi) exhibits a unique structure, defining a non-symmorphic space group 1) protecting the four-fold degeneracy of the nodal line no matter SOC is present or not; 2) introducing linear dispersion relations at the vicinity of the nodal line. This guarantees the robust DNL electronic phase without any orbital and element dependence. With this inherent relation, we expect and theoretically prove the generality of the robust DNL in a series of 2D layers that are isostructural to 3-ALs Bi. This opens the door towards growth, exploration and utilization of intrinsic 2D DNL materials. In the 3-ALs Bi case, the DNL state is near the Fermi level (E_F) and is rather neat that other trivial bands open a gap around the E_F , making the 3-ALs Bi one of the “cleanest” DNL semimetal (DNLs) ever proposed.

Main

Condensed matter physics is witnessing a rapid expansion of materials with Dirac fermion low-energy excitations. The seemingly diverse materials share the similarity of possessing four-fold degenerate Dirac nodes normally protected by certain crystalline symmetries except at 3D Weyl points, where it degrades into two-fold by breaking the **I.T.** (**I** and **T** represent the central inversion and time reversal operations, respectively) symmetry^{2-6,13-15}. In particular cases of three-dimensional (3D) materials, a combination of **I.T.** and mirror-glide symmetry could protect four-fold degenerate Dirac nodal points (DNPs) into a continuous line in the momentum space, accomplishing DNL phases^{4-6,16-20}. If a DNL spans across the E_F , a more specialized DNL phase, i.e. DNL semimetal (DNLS) state, emerges. The DNLS state hosts robust fermionic excitations around the band-crossing point for exploring unusual electronic²¹⁻²³, optical²⁴⁻²⁶ and magnetic behaviors^{27,28}. While inclusion of SOC usually gap out DNL states and the four-fold DNL often degrades to 2+2 ones under SOC^{5,11,16,18,29,30}. Although it was argued that the four-fold degeneracy could be approximately achieved in materials comprised of lighter elements where the effects of SOC are weak^{7,8,11,18,31,32}.

It is the same in the 2D systems where the nodal lines in experimentally observed or theoretically predicted 2D DNLSs gap out under strong SOC⁷⁻¹¹. Recently, it has been theory predicted^{9,32,33} and experiment proved¹¹ that, in some 2D structures, non-symmorphic symmetry involving fractional lattice translations does protect the four-fold degeneracy of DNPs at certain isolated k points against SOC. However, none of those DNPs extends to a DNL under SOC in any real 2D material. Here, we experimentally and theoretically show that a three mono-atomic layers (3-ALs) Bi grown on BP crystal substrates, a novel phase of Bi, is a robust four-fold DNLSs against SOC, protected by the non-symmorphic $C_{2v} \times Z_2^T$ symmetry. The existence of the DNL state was experimentally identified using scanning tunneling spectroscopy (STS) quasi particle interference (QPI) techniques, We further demonstrated that 3-ALs Bi features a non-trivial edge state coexisting with DNL, which is usually not presented in symmetry protecting DNLSs. The SOC-robust DNL electronic phase is guaranteed by

the crystalline structure of the 3-ALs Bi as predicted by group theory analysis and revealed by density functional theory (DFT) calculations. These findings serve as a solid example to illustrate the essential symmetry physics of protecting DNLSs. Because the crystalline structure of 3-ALs Bi is strongly related with the substrate diatomic layers (2-ALs) BP-like structure, we suggest that the discovery of the novel Bi phase and its DNLS state in this work could be imposed to most VA group elements with possible extension to other 2D systems to create intrinsic DNLSs in real materials.

We grew bismuth nano-islands on a single crystal BP surface (Fig. 1a inset). The islands prefer a belt like shape with the longer side oriented along the zigzag (ZZ) azimuth of

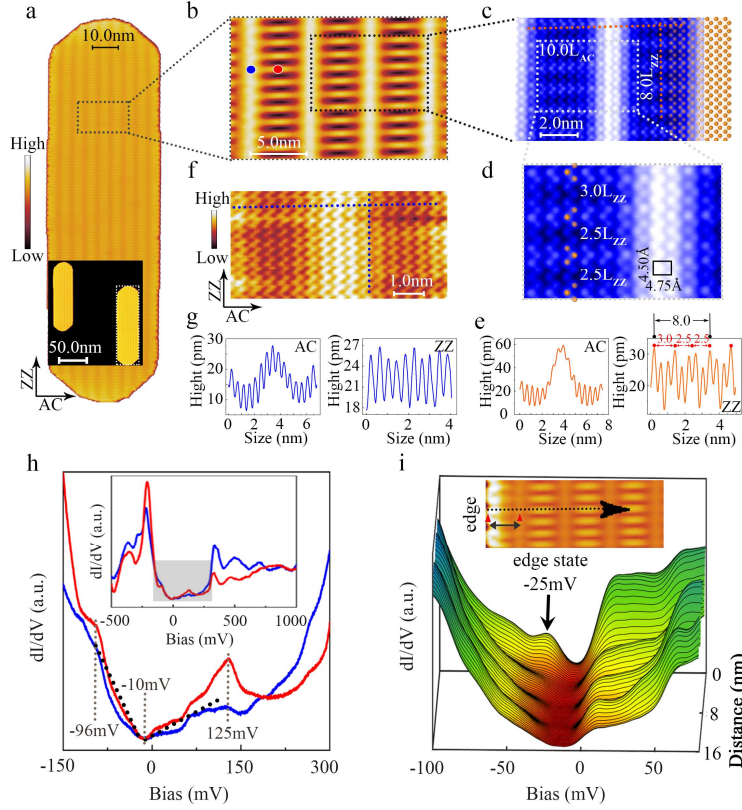


Fig. 1 | Atomic structure and electronic spectra of the Bi (110) thin films. **a**, STM image ($V_{\text{bias}} = +400$ mV, $I_t = 100$ pA) of a typical Bi island. The inset shows an area consisting two islands. **b**, The highlight of the STM contrast inside the rectangle area in (a). **c**, Atom-resolved STM image ($V_{\text{bias}} = +100$ mV, $I_t = 100$ pA) of the rectangle area in (b). Atomic ZZ chains are clearly resolved. The dotted white rectangle represents the unit of the superlattice ladder with $8L_{\text{ZZ}} \times 10L_{\text{AC}}$. **d**, An amplified image highlights the STM contrast within one unit of the superlattice. The oranges balls are markers representing the appearing orientation of the ZZ contrast of the Bi atoms. The black rectangle shows the lattice constants of the Bi (110) unit cell. **e**, The line profiles along ZZ and AC direction cutting at the orange dashed lines in (c). **f**, Q-plus AFM image of the superlattice. **g**, The line profiles along ZZ and AC direction cutting at the blue dashed lines in (f). **h**, dI/dV spectra acquired on two typical locations (blue and red dots in (b)) in the center of an island. The inset shows the spectra with bigger bias range. **i**, dI/dV spectra acquired along the line perpendicular to the edge (black arrow on the inset STM image).

the underlying BP, exhibiting a clear Bi (110) structure (Extended Data Fig.1). Each island appears a ladder shape (Fig. 1b) in STM images consisting of ~ 11.5 Å horizontally and ~ 50.0 Å vertically spaced bright stripes, adopting an 8 (zigzag, ZZ) \times 10 (armchair, AC) superlattice structure on BP (Fig. 1c). The 8 times zigzag period

($8L_{ZZ}$) is further dividable into three sub-periods with 3, 2.5 and 2.5 times L_{ZZ} (Fig. 1d and Fig. 1e); this is a primarily electronic effect because of the missing sub-periods in nc-AFM images (Fig. 1f and Fig. 1g). It is, most likely, an electronic Moiré pattern in the ZZ direction³⁷. On the other hand, basing on the AFM data (Fig. 1g), the 10 times armchair period ($10L_{AC}$) is derived from an-appreciable atomic corrugation along the AC direction. The Bi (110) thin films were generally thought grown with a 2-ALs BP-like model on different substrates³⁴⁻⁴⁰. Nevertheless, the apparent heights of our islands, acquired at different bias voltages, center around 9.60 Å (Extended Data Fig. 2). This value is, however, inconsistent with the 2-ALs BP-like model (6.60 Å to 7.00 Å)⁴¹⁻⁴⁴ but suggests a 3-ALs Bi structure, requiring to a closer examination on those islands.

The islands show a semi-metallic character and a robust edge state, which is, together with the ladder-like STM contrast, substantially different from those of previously found in the 2-ALs BP-like Bi (110) thin-films or islands. Those structures show uniform STM contrast and the STS spectroscopy is either the topological insulator character with edge states^{35,38} or semi-metallic character without any edge state^{39,40}. Figure 1h depicts typical dI/dV STS spectra acquired on different locations at the center of an island. Despite on different STM contrast, the spectra show similar features (Inset in Fig. 1h). Zoomed into the energy range around E_F , the spectra consistently exhibit an asymmetric V-shaped dip centering at -10 mV and spanning from -96 mV to +125 mV. The V-shaped differential conductivity indicates that the measured local density of state (LDOS) could be attributed to a 2D Dirac system, as what has been revealed in the prototype example of graphene⁴⁵⁻⁴⁹. When the acquiring position approaches an edge of the island, a new peak sitting around -25 mV fades in (Fig. 1i). The new state mainly locates at the edges of the island with a penetration depth of ~ 38.0 Å (Extended Data, Fig. 3). As both the dip and the edge state are reproducible and independent of the width of the islands (Extended Data, Fig. 3), their origin of quantum confinement effect is ruled out.

All these results compellingly indicate that our islands grown on BP are, most likely, a novel allotrope of Bi. This is reinforced by our DFT calculations. Given the apparent height of ~ 9.6 Å, our DFT considered four 3 ALs- Bi structures and reveals the most likely structure showing its perspective and side-views in Fig. 2a and 2b. This structure is, at least 40 meV/Bi more stable than other three considered 3-ALs Bi (110) stacking structures and becomes even more stable in thicker layers (Extended Data Fig. 4 and Extended Data Table 1), reinforcing the reliability of this structure. It is slightly prone to transform into a combined half 2-ALs plus half 4-ALs hetero-layer in the free-standing form, but could be stabilized using a single crystal BP substrate (Extended Data Table 1). In this 3-ALs Bi, the top and bottom Bi mono-atomic layers form two oppositely oriented BP-like layers shared by the middle mono-atomic layer, respectively. It thus adopts a Bi (110)-like surface structure with a rectangle lattice. The sideview of it appears a wall tessellated by vertically oriented bricks, we thus name this new allotrope as the ``brick phase”.

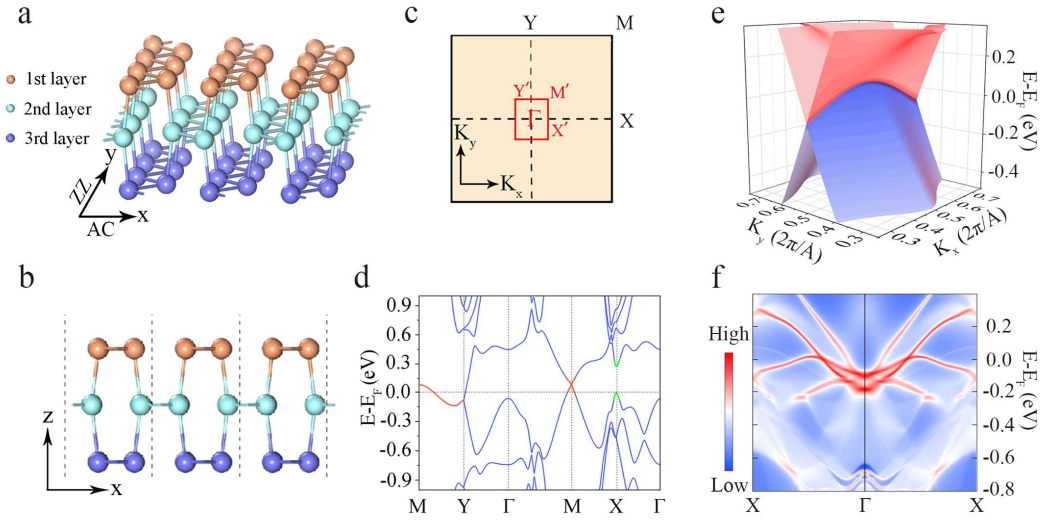


Fig. 2 | Atomic structure and band structure of 3-ALs Bi. **a, b,** Top (a) and side (b) views of the atomic structure of 3-ALs Bi (110). **c,** Corresponding schematic 1st BZ. The red colored BZ represents the Bi (110) superlattice. **d,** Electronic band structures of 3-ALs Bi along high-symmetry directions with SOC. The Dirac cone at the M point and the Dirac nodal line along Y-M are highlighted by red color. The green curves represent the SOC opening gap at the X point. **e,** plot of a 3D electronic band surface of 3-ALs Bi with SOC. **f,** Edge state of 3-ALs Bi along AC direction.

Figure 2d shows the electronic band structure under SOC of the 3-ALs Bi. The 3-ALs brick phase is a semimetal with a gap opening around time-reversal invariant point X (green angles). Within the bandgap, a four-fold degenerated Dirac point was identified at the M point (the red cross), which extends to all momenta along the entire Y-M line forming a DNL (the red curve). We plotted a 3D electronic band structure of the DNL in Fig. 2e to more clearly show this unique DNL, which illustrates the linear dispersion relations along other directions and four-fold Dirac bands degenerated in the Y-M line. In comparison with the band structure without SOC⁴¹, the SOC only flattens the DNL dispersion, indicating the robustness of the DNL state in the 3-ALs Bi. Given the bandgap at X, there is no other trivial band existing in part of the energy window of the DNL, i.e. from 0 to +80 meV, giving rise to a rare “neat” DNL state around E_F . In addition, theoretical analysis shows a band inversion occurring around the X point, resulting the 3-ALs Bi to have nontrivial edge states at its boundary⁴¹. Figure 2f plots the edge states in the Γ -X direction, which yields few clear and flat edge states just

below E_F . This result is highly consistent with the experimentally observed edge state of our Bi islands (Fig. 1i). The results confirm the assessment of the 3-ALs brick phase and attribute the experimentally observed edge state as the topologically nontrivial edge state origin. Thus a nontrivial edge state coexists with the DNL in this 3-ALs brick phase Bi allotrope.

This unique DNL state is expected to be observed in the grown 3-ALs Bi islands. Our DFT calculations fully reproduced the experimental $8L_{ZZ} \times 10L_{AC}$ 3-ALs Bi superlattice in the model shown in Fig 3a. A smooth vertical corrugation of 8-16 pm is found along the AC direction, consistent with the AFM results (Fig. 1f). Figure 3b shows a simulated STM contrast, which well reproduces the high-low contrasts along the ZZ direction and resolve the three sub-periods within the $8L_{ZZ}$ (Fig. 3c). These results, again, support the reliability of our DFT structure. The corrugations are not solely the bottom Bi atoms' business that they are well followed by the middle and top layer Bi atoms (Extended Data Fig. 5) in 3-ALs Bi. Thus, the grown Bi thin film shares the same symmetry with the free-standing 3-ALs Bi, except some substrate perturbations as elucidated later.

Because of the $8L_{ZZ} \times 10L_{AC}$ 3-ALs Bi superlattice formed on BP substrate, the original unit-cell BZ of the free-standing 3-ALs Bi folds to an eight- and ten-times smaller superlattice BZ (SLBZ, Fig. 2c). We use X' , Y' , M' to represent the boundary of the SLBZ. In this BZ, the original Y-M line, where the DNL develops, folds to the $\Gamma-X'$ line, along which the DNL scatters several times appearing rhombus-like shapes in the band structure plotted in Fig. 3d and 3e. In Fig. 3d the green triangles highlight the rhombus formed by the pure DNL after folding. In Fig. 3e, the red dots highlight the DNL which hybridizes with the p_z orbitals of P atoms underneath in certain energy window. As a result, the DNL slightly lifts the fourfold degeneracy and leads to a tiny but appreciable splitting. The folding DNL state complicates its appearance in the k -space; this hinders probing the DNL using angle-resolved photoemission spectroscopy (ARPES), which has not been successful yet. However, such band folding provides a

feasible chance of utilizing the STS-QPI approach^{50,51} to characterize the DNL state from real-space.

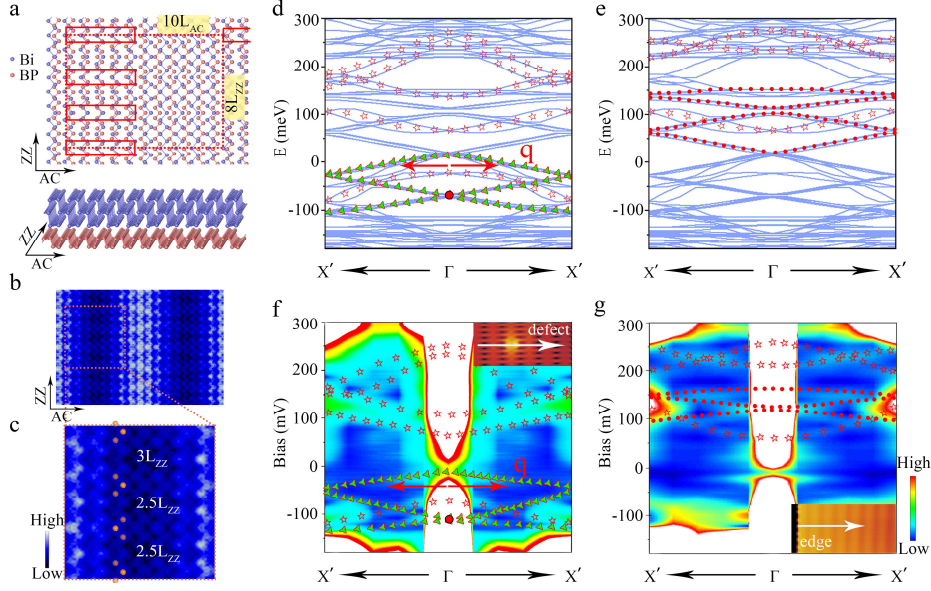


Fig. 3 | Atomic model and E-q dispersions of the folded Dirac nodal lines in 3-ALs Bi (110) on BP surface. **a**, Atomic model structure of the $8L_{ZZ} \times 10L_{AC}$ Bi (110) superlattice. The red dotted-rectangle corresponds the superlattice. **b**, Simulated STM image of the superlattice ($V_{bias} = +100$ mV). **c**, The amplified image highlights the simulated STM contrast of the Bi atoms. The oranges balls are markers representing the STM contrast orientation of the Bi ZZ chain. **d**, Band structures along the $X'-\Gamma-X'$ direction of the superlattice highlighting the folded pure DNL state by green triangles. **e**, Band structures along the $X'-\Gamma-X'$ direction of the superlattice highlighting the folded hybridized DNL state by red dots. The red hollow stars represent the electronic bands not related to the DNL state but observable in the experiments. The same scheme of markers was applied to (f) and (g). Compared with the experimental dI/dV spectra, DFT calculations lift all states by a 0.028 eV, which is comparable with other experiments. **f**, **g**, E-q dispersions along $X'-\Gamma-X'$ obtained from QPI scattering by the surface defect (f) or by the edge (g) by performing FFT on the corresponding series dI/dV spectra. In the QPI patterns, the obtained wave vector q represents allowed scatterings of the electron Bloch waves from the initial state of k_i to the final state k_f .

Our QPI spectra well confirm the theoretically predicted DNL in the 3-ALs Bi superlattice. Figure 3f depicts the QPI revealed E-q relations along the $X'-\Gamma-X'$ line by acquiring continuous STS spectra (Extended Data Fig. 6) across a typical surface defect along the x (AC) direction. It, guiding by green triangles, clearly shows several bands exhibiting nearly linear relations which construct the rhombus folded by the pure DNL

state (from -140 mV to -10 mV). The QPI acquired at edges (Fig. 3g) of the islands have a stronger scattering strength and thus yield sharper contrast, especially for those DNL states hybridizing with the substrate (red dots in Fig. 3e). In this case, the rhombuses-shaped band dispersions are observed from 90 mV to 145 mV. These features are within the energy windows of the folded hybridized DNL from 10 meV to 152 meV as predicted with DFT (red dots in Fig. 3e).

Similar measurements, revealing the E-q relations along $Y'-\Gamma-Y'$ (the ZZ direction, Extended Data Fig. 7), further validate our STS-QPI measurements along $X'-\Gamma-X'$. The appearance of E-q relations in STS-QPI highly depends on the type of surface defects, which is, most likely, resulted from the existence of periodically atomic corrugations in the Bi islands and the complicated hybridization of DNL with the substrate. Nevertheless, our QPI results performed across the surface defect and from the edge are complementary to reveal their DNL origin, which unambiguously demonstrated direct observations of DNL in 3-ALs Bi.

Space group theory analysis elucidates the detailed symmetries protecting the DNL state in 3-ALs Bi. The symmetry of 3-ALs Bi is described by the non-symmorphic space group $Pmma$, whose point group $G = D_{2h} \times Z_2^T$ is generated by C_{2x} , C_{2y} , M_z and \tilde{T} with $\tilde{T} = IT$. As the combined operation $\tilde{T} = IT$ with $\tilde{T}^2 = -1$ guarantees a two-fold Kramers degeneracy in the spin degrees of freedom at any k point, in order to obtain a DNL, the extra 2-fold degeneracy needs to come from orbital degrees of freedom. We found that the non-symmorphic $C_{2v} \times Z_2^T$ group ($\{C_{2x}|(0, 1/2, 0)\}$ and $\{M_y|(0, 1/2, 0)\}$) in 3-ALs Bi is the exact symmetry to protect the two-fold orbital degeneracy along the Y-M ($k_x, \pi, 0$) line no matter SOC is present or not. Figure 4a, 4b and 4c, 4d illustrates the symmetry operation of $\{C_{2x}|(0, 1/2, 0)\}$ and $\{M_y|(0, 1/2, 0)\}$ respectively. Without SOC these two operations are commute with each other but are anti-commute with the I.T symmetry along Y-M, offering two double orbital degenerations (Fig. 4e). By including SOC, $\{C_{2x}|(0, 1/2, 0)\}$ is still anti-commute with I.T., resulting a two-fold orbital degeneracy. However, $\{C_{2x}|(0, 1/2, 0)\}$ and $\{M_y|(0, 1/2, 0)\}$ becomes anti-

commute along Y-M; this additional anti-commute relation protects spin degeneracy.

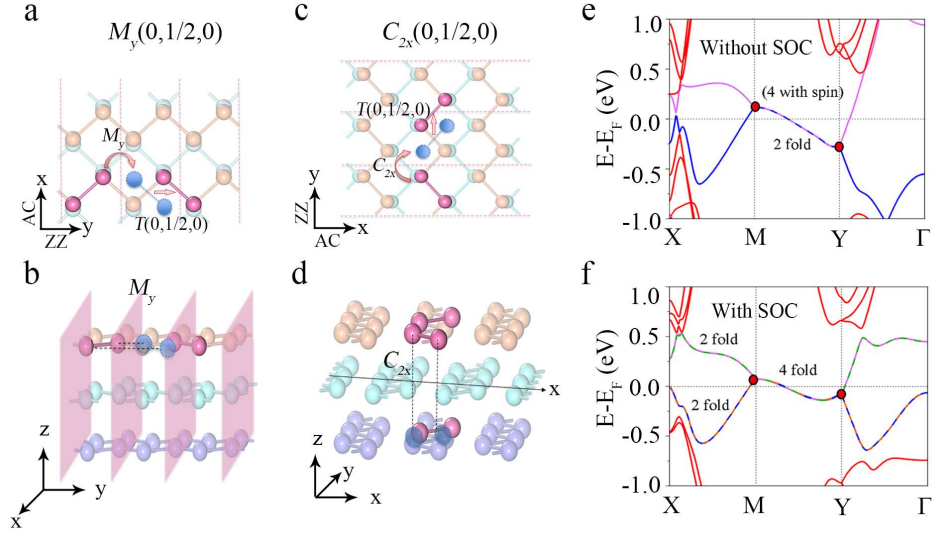


Fig. 4 | Space group symmetry analysis of 3-ALs Bi. **a, b,** The atomic model shows operations of $[C_{2x}] (0, 1/2, 0)$ from the top (a) and side (b) views of 3-ALs Bi. The pink atoms represent the initial and final positions of Bi atoms involved in the operation and the light-blue atoms represent the transition positions of the atoms before taking the fractional lattice transition. **c, d,** The atomic model shows operations of $\{M_y\} (0, 1/2, 0)$ from the top (c) and side (d) views of 3-ALs Bi. **e, f,** Band structures of 3-ALs Bi centering along Y-M without (e) and with (f) SOC. Curves of mixed pink and blue colors represent the origin of the fourfold degenerate DNL bands in both cases.

As a result, the quadruple degeneracy along Y-M is thus kept under SOC (Fig. 4f). The results indicate that the nonsymmorphic symmetry play a pivotal role in protecting the quadruple degeneracy against SOC in 2D systems. We further proved that all these states are of linear dispersion relation guaranteeing their character of Dirac states⁴¹.

This structural symmetry is, to the best of our knowledge, the exact one in 2D that intrinsically offers quadruple-degenerated DNL⁴¹. The DNL is symmetry protected, i.e., it is independent of specific orbital and does not need band inversion. Therefore, the DNL is an inevitable occurrence in each system that satisfies the above symmetry, which could be imposed by most VA group elements with possible extension to other 2D systems. Our DFT calculations verified that 1- and 5-ALs Bi, 3-ALs P, As and Sb are all DNLs against SOC⁴¹. Experimentally, we have observed similar STM ladder contrasts and robust edge states in 5-ALs Bi, proving the DNLs are symmetrically

guaranteed (Extended Data Fig. 8). We also expect less substrate influence to DNL in 5-ALs or thicker Bi thin films than those in the 3-ALs crystal.

On the basis of STM experiments, first principle calculations and symmetry analysis, we discovered a symmetry guaranteed simple 2D DNLS in the rationally designed and artificially built 3-ALs Bi brick phase thin-films. It is a novel allotrope of Bi few-layers and the DNL is immune to very strong SOC. In fact, strong SOC becomes an advantage enriching the electronic characters in the 3-ALs Bi brick phase rather than degrading the four-fold degeneracy of the DNL. First, the strong SOC of the Bi element results in a small dispersion of the DNL around E_F . Second, the SOC opens a gap around E_F , which making part of the DNL neat without any interference with other states. These two results would facilitate the probe and manipulation of the physical behaviors essentially governed by the fermionic excitations around protected Dirac nodes. Third, the strong SOC introduces a band-inversion induced non-trivial edge state in 3-ALs Bi. Its first time's coexistence with the symmetry guaranteed DNL within one system provides additional degrees of freedom where the two could be individually manipulated and/or interacted by external perturbations to produce emergent Dirac states.

We emphasize that the DNL in 3-ALs Bi is solely symmetry dictated. This implies 1) its generality in a series of 2D layers with iso-structure as that of the 3-ALs Bi brick phase. Because BP substrates favors of the formation of this unique 3-ALs Bi brick structure, we speculate realization of similar brick phase for most VA group elements to boost experimental achievement of intrinsic 2D DNLSs; 2) its robustness against lattice distortions that keeps the nonsymmorphic symmetry. Experimentally, narrow-width 3-ALs Bi islands are created in which the surface stress fully releasing along the AC-direction (Extended Data Fig. 9). Such narrow islands exhibit similar LDOS as those of 3-ALs Bi superlattice. Moreover the narrow islands reveal a well-defined V-shaped differential conductivity compared with that of Bi superlattice and offer mysterious S or O-like 1D electronic states that are subject to future investigations. All

these intriguing properties compellingly provide that the discovered 3-ALs Bi brick phase holds promise as a new platform for future exploring the fundamental Dirac states physics.

Methods

Sample preparation and STM/STS measurements. The BP crystals are home-grown using a chemical vapor transport (CVT) method (red phosphorus, tin iodide (SnI_4), and tin powders as the starting materials) in a two-zone tube furnace in a temperature gradient of 600°C to 540°C . The STM and spectroscopy experiments are carried out in an ultrahigh vacuum low temperature STM system (CreaTec). Prior to STM experiments, the BP crystals are cleaved *in-situ* in a preparation chamber under ultrahigh vacuum at room temperature (RT). Bismuth atoms (99.999% purity, Aldrich) are evaporated from a resistively heated evaporator onto a freshly prepared BP surface. The BP substrates are kept at ambient temperature during the evaporation. The prepared sample is then immediately transferred into the STM chamber, and cooled down to 77 K and/or 4.5 K. STM topographic images are acquired in the constant-current mode. The dI/dV spectra are measured using the standard lock-in technique with a bias modulation of 8 mV at 321.333 Hz. The STM tips are chemically etched tungsten or mechanically cut Pt-Ir wires, which are further calibrated spectroscopically against the Shockley surface states of cleaned Cu (111) or Au (111) surfaces before being utilized on Bi islands/BP.

DFT calculations. DFT calculations were performed using the generalized gradient approximation for the exchange-correlation potential, a plane-wave basis, and the projector augmented wave method set as implemented in the Vienna *ab-initio* simulation package (VASP)⁵²⁻⁵⁴. The energy cutoff for plane wave was set to 650 and 350 eV for variable volume structural relaxation of pure Bi 2D materials and invariant volume structural relaxation of Bi island on BP surface. For freestanding Bi layers, the k-points sampling of the first Brillouin zone is $14 \times 14 \times 1$, generated automatically by Monkhorst-Pack method⁵⁵. The k-points sampling is with only the Γ -point for Bi island on BP surface. The vacuum layers of all supercells are larger than 15 Å. The bottom BP layer were kept fixed and all other atoms were fully relaxed until the residual force per atom was less than 0.05 eV/Å during the relaxations of Bi island on BP surface and less than 0.001 eV/Å during all the other structural relaxations. In structural relaxation

and electronic property calculations, DFT-D3 correction method is considered with the Perdew-Burke-Ernzerhof (PBE) exchange functional (PBE-D3)^{56,57}. The Bi-BP superstructure was modeled using a superlattice consisting of a $8L_{zz} \times 10L_{ac}$ Bi 3-AL and $11L_{zz} \times 11L_{ac}$ BP 2-AL with a 15 Å vacuum layer perpendicular to the Bi and BP layers. All electronic properties of the superlattice were calculated with the consideration of SOC. The STM simulation was performed using the Tersoff-Hamann method⁵⁸. The edge states are calculated using Wannier90⁵⁹ and WannierTools⁶⁰.

Data availability: The data that support the findings of this study are available from the corresponding authors upon request.

Acknowledgement

We gratefully acknowledge fruitful discussions with Haiwen Liu, Hongjian Du, Shaochun Li, Rui Yu, Chunwei Lin, Hongming Weng and Xi Dai. This work is supported by the National Key R&D Program of China (Grant Nos. 2017YFA0303500, 2017YFA0303504, 2018YFE0202700); the Strategic Priority Research Program of Chinese Academy of Sciences (Grant No. XD30000000), the National Natural Science Foundation of China (Grant Nos. 11774267, 61674171 and 11974422). the Fundamental Research Funds for the Central Universities and the Research Funds of Renmin University of China [Grants No. 16XNLQ01 and No. 19XNQ025 (W.J.)]. The contributions from H.P. thank the Luo Jia Visiting Chair Professorship in Wuhan University. Calculations were performed at the Physics Lab of High-Performance Computing of Renmin University of China and Shanghai Supercomputer Center.

Author Contributions

X.X.C, Y.F.L and C.C.L grew the Bi samples and performed STM measurements; D.P.G. and W.J. performed first principle calculations; P.J.G., Z.X.L and W.J. conducted the symmetry analysis; G.Q.Mei and L.M.C. grew the BP crystals; M.F. and L.M.C initiated the project and experiments; W.J. conceived the theoretical calculations and analysis; C.L. and S.J.Tan. participated in experiments of electronic structure

studies; K.L. and Z.Y.L. participated in data analysis and discussions; M.F., W.J., H.P. and L.M.C. analyzed the data, and wrote the manuscript with input from all authors.

Additional information

Additional data related to this paper are available from the corresponding authors upon request.

Competing interests: The authors declare that they have no competing interests.

References

- 1 Landau, L. D. On the theory of phase transitions. I. *Zh. Eksp. Teor. Fiz.* **11**, 19 (1937).
- 2 Novoselov, K. S. *et al.* Two-dimensional gas of massless Dirac fermions in graphene. *Nature* **438**, 197-200 (2005).
- 3 Wehling, T. O., Black-Schaffer, A. M. & Balatsky, A. V. Dirac materials. *Adv. Phys.* **63**, 1-76 (2014).
- 4 Mullen, K., Uchoa, B. & Glatzhofer, D. T. Line of Dirac Nodes in Hyperhoneycomb Lattices. *Phys. Rev. Lett.* **115**, 026403 (2015).
- 5 Kim, Y., Wieder, B. J., Kane, C. L. & Rappe, A. M. Dirac Line Nodes in Inversion-Symmetric Crystals. *Phys. Rev. Lett.* **115**, 036806 (2015).
- 6 Wang, S.-S., Liu, Y., Yu, Z.-M., Sheng, X.-L. & Yang, S. A. Hourglass Dirac chain metal in rhenium dioxide. *Nat. Commun.* **8**, 1844 (2017).
- 7 Feng, B. *et al.* Experimental realization of two-dimensional Dirac nodal line fermions in monolayer Cu₂Si. *Nat. Commun.* **8**, 1007-1012 (2017).
- 8 Gao, L. *et al.* Epitaxial Growth of Honeycomb Monolayer CuSe with Dirac Nodal Line Fermions. *Adv. Mater.* **30**, 1707055 (2018).
- 9 Kowalczyk, P. J. *et al.* Realization of Symmetry-Enforced Two-Dimensional Dirac Fermions in Nonsymmorphic α -Bismuthene. *ACS Nano* **14**, 1888-1894 (2020).
- 10 Jin, K.-H., Huang, H., Wang, Z. & Liu, F. A 2D nonsymmorphic Dirac semimetal in a chemically modified group-VA monolayer with a black phosphorene structure. *Nanoscale* **11**, 7256-7262 (2019).
- 11 Li, L., Kong, X. & Peeters, F. M. New nanoporous graphyne monolayer as nodal line semimetal: Double Dirac points with an ultrahigh Fermi velocity. *Carbon* **141**, 712-718 (2019).
- 12 Dirac, P. A. M. The quantum theory of the electron. *Proc. R. Soc. A* **117**, 610-624 (1928).
- 13 Yang, S. A., Pan, H. & Zhang, F. Dirac and Weyl Superconductors in Three Dimensions. *Phys. Rev. Lett.* **113**, 046401 (2014).
- 14 Liu, Z. K. *et al.* Discovery of a Three-Dimensional Topological Dirac Semimetal, Na₃Bi. *Science* **343**, 864-867 (2014).
- 15 Wieder, B. J., Kim, Y., Rappe, A. M. & Kane, C. L. Double Dirac Semimetals in Three Dimensions. *Phys. Rev. Lett.* **116**, 186402 (2016).
- 16 Yu, R., Weng, H., Fang, Z., Dai, X. & Hu, X. Topological Node-Line Semimetal and Dirac Semimetal State in Antiperovskite Cu₃PdN. *Phys. Rev. Lett.* **115**, 036807 (2015).
- 17 Belopolski, I. *Discovery of Magnetic Topological Crystals*, Princeton University, (2019).
- 18 Fu, B.-B. *et al.* Dirac nodal surfaces and nodal lines in ZrSiS. *Sci. Adv.* **5**, eaau6459 (2019).
- 19 Schoop, L. M. *et al.* Dirac cone protected by non-symmorphic symmetry and three-dimensional Dirac line node in ZrSiS. *Nat. Commun.* **7**, 11696 (2016).
- 20 Bian, G. *et al.* Topological nodal-line fermions in spin-orbit metal PbTaSe₂. *Nat. Commun.* **7**, 10556 (2016).
- 21 Shao, Y. *et al.* Electronic correlations in nodal-line semimetals. *Nat. Phys.* **16**, 636-641 (2020).

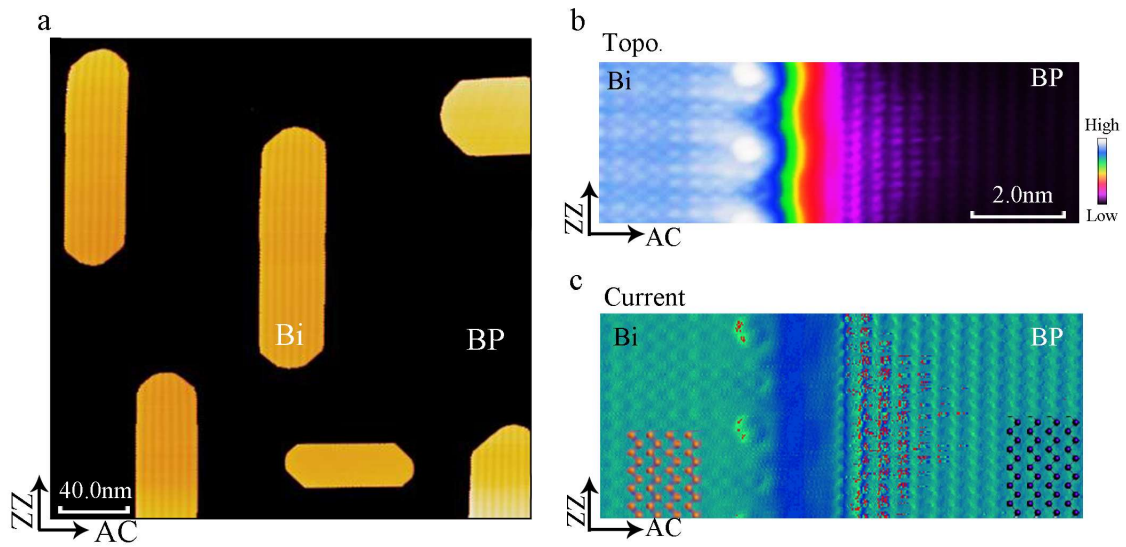
- 22 Pezzini, S. *et al.* Unconventional mass enhancement around the Dirac nodal loop in ZrSiS. *Nat. Phys.* **14**, 178-183 (2018).
- 23 Muechler, L. *et al.* Superconducting order parameter of the nodal-line semimetal NaAlSi. *APL Mater.* **7**, 121103 (2019).
- 24 Muñoz-Segovia, D. & Cortijo, A. Many-body effects in nodal-line semimetals: Correction to the optical conductivity. *Phys. Rev. B* **101**, 205102 (2020).
- 25 Scherer, M. M. *et al.* Excitonic instability and unconventional pairing in the nodal-line materials ZrSiS and ZrSiSe. *Phys. Rev. B* **98**, 241112 (2018).
- 26 Martín-Ruiz, A. & Cortijo, A. Parity anomaly in the nonlinear response of nodal-line semimetals. *Phys. Rev. B* **98**, 155125 (2018).
- 27 Voerman, J. A. *et al.* Origin of the butterfly magnetoresistance in ZrSiS. *Phys. Rev. Mater.* **3**, 084203 (2019).
- 28 Laha, A. *et al.* Magnetotransport properties of the correlated topological nodal-line semimetal YbCdGe. *Phys. Rev. B* **99**, 241102 (2019).
- 29 Chan, Y. H., Chiu, C.-K., Chou, M. Y. & Schnyder, A. P. Ca₃P₂ and other topological semimetals with line nodes and drumhead surface states. *Phys. Rev. B* **93**, 205132 (2016).
- 30 Topp, A. *et al.* Surface Floating 2D Bands in Layered Nonsymmorphic Semimetals: ZrSiS and Related Compounds. *Phys. Rev. X* **7**, 041073 (2017).
- 31 Fang, C., Chen, Y., Kee, H.-Y. & Fu, L. Topological nodal line semimetals with and without spin-orbital coupling. *Phys. Rev. B* **92**, 081201 (2015).
- 32 Zhou, S. Y. *et al.* Origin of the energy bandgap in epitaxial graphene. *Nat. Mater.* **7**, 259-260 (2008).
- 33 Young, S. M. & Kane, C. L. Dirac Semimetals in Two Dimensions. *Phys. Rev. Lett.* **115**, 126803 (2015).
- 34 Kowalczyk, P. J. *et al.* STM and XPS investigations of bismuth islands on HOPG. *Suf. Sci.* **605**, 659-667 (2011).
- 35 Lu, Y. *et al.* Topological Properties Determined by Atomic Buckling in Self-Assembled Ultrathin Bi(110). *Nano Lett.* **15**, 80-87 (2015).
- 36 Kowalczyk, P. J. *et al.* Electronic Size Effects in Three-Dimensional Nanostructures. *Nano Lett.* **13**, 43-47 (2013).
- 37 Gou, J. *et al.* The effect of moiré superstructures on topological edge states in twisted bismuthene homojunctions. *Sci. Adv.* **6**, eaba2773 (2020).
- 38 Sun, J.-T. *et al.* Energy-Gap Opening in a Bi(110) Nanoribbon Induced by Edge Reconstruction. *Phys. Rev. Lett.* **109**, 246804 (2012).
- 39 Peng, L. *et al.* Unusual Electronic States and Superconducting Proximity Effect of Bi Films Modulated by a NbSe₂ Substrate. *ACS Nano* **13**, 1885-1892 (2019).
- 40 Liu, J.-Y. *et al.* Scanning tunneling microscopy research of Bi (110) thin films grown on NbSe₂. *Acta. Phys. Sin.* **67**, 170701.
- 41 Dong, X. *et al.* Epitaxial Growth and Structural Properties of Bi(110) Thin Films on TiSe₂ Substrates. *J. Phys. Chem. C* **123**, 13637-13641 (2019).
- 42 Hu, T. *et al.* Nanostructured Bi Grown on Epitaxial Graphene/SiC. *J. Phys. Chem. Lett.* **9**, 5679-5684 (2018).

- 43 Kawakami, N. *et al.* Structural evolution of Bi thin films on Au(111) revealed by scanning tunneling microscopy. *Phys. Rev. B* **96**, 205402 (2017).
- 44 Mahapatra, O. A scanning probe microscopy (SPM) study of Bi (110) nanostructures on highly oriented pyrolytic graphite (HOPG). (2013).
- 45 Gao, L., Guest, J. R. & Guisinger, N. P. Epitaxial Graphene on Cu(111). *Nano Lett.* **10**, 3512-3516 (2010).
- 46 Pan, Y. *et al.* Highly Ordered, Millimeter-Scale, Continuous, Single-Crystalline Graphene Monolayer Formed on Ru (0001). *Adv. Mater.* **21**, 2777-2780 (2009).
- 47 Li, G., Luican, A. & Andrei, E. Y. Scanning Tunneling Spectroscopy of Graphene on Graphite. *Phys. Rev. Lett.* **102**, 176804 (2009).
- 48 Qin, Z. *et al.* Direct Evidence of Dirac Signature in Bilayer Germanene Islands on Cu(111). *Adv. Mater.* **29**, 1606046 (2017).
- 49 Li, G. & Andrei, E. Y. Observation of Landau levels of Dirac fermions in graphite. *Nat. Phys.* **3**, 623-627 (2007).
- 50 Zhu, Z. *et al.* Quasiparticle interference and nonsymmorphic effect on a floating band surface state of ZrSiSe. *Nat. Commun.* **9**, 4153 (2018).
- 51 Drozdov, I. K. *et al.* One-dimensional topological edge states of bismuth bilayers. *Nat. Phys.* **10**, 664-669 (2014).
- 52 Blöchl, P. E. Projector augmented-wave method. *Phys. Rev. B* **50**, 17953-17979 (1994).
- 53 Kresse, G. & Joubert, D. From ultrasoft pseudopotentials to the projector augmented-wave method. *Phys. Rev. B* **59**, 1758-1775 (1999).
- 54 Kresse, G. & Furthmüller, J. Efficient iterative schemes for ab initio total-energy calculations using a plane-wave basis set. *Phys. Rev. B* **54**, 11169-11186 (1996).
- 55 Monkhorst, H. J. & Pack, J. D. Special points for Brillouin-zone integrations. *Phys. Rev. B* **13**, 5188-5192 (1976).
- 56 Grimme, S., Antony, J., Ehrlich, S. & Krieg, H. A consistent and accurate ab initio parametrization of density functional dispersion correction (DFT-D) for the 94 elements H-Pu. *J. Chem. Phys.* **132**, 154104 (2010).
- 57 Perdew, J. P., Burke, K. & Ernzerhof, M. Generalized Gradient Approximation Made Simple. *Phys. Rev. Lett.* **77**, 3865-3868 (1996).
- 58 Hansma, P. K. & Tersoff, J. Scanning tunneling microscopy. *J. Appl. Phys.* **61**, R1-R24 (1987).
- 59 Mostofi, A. A. *et al.* An updated version of wannier90: A tool for obtaining maximally-localised Wannier functions. *Comput. Phys. Commun.* **185**, 2309-2310 (2014).
- 60 Wu, Q., Zhang, S., Song, H.-F., Troyer, M. & Soluyanov, A. A. WannierTools: An open-source software package for novel topological materials. *Comput. Phys. Commun.* **224**, 405-416 (2018).

Extended Data

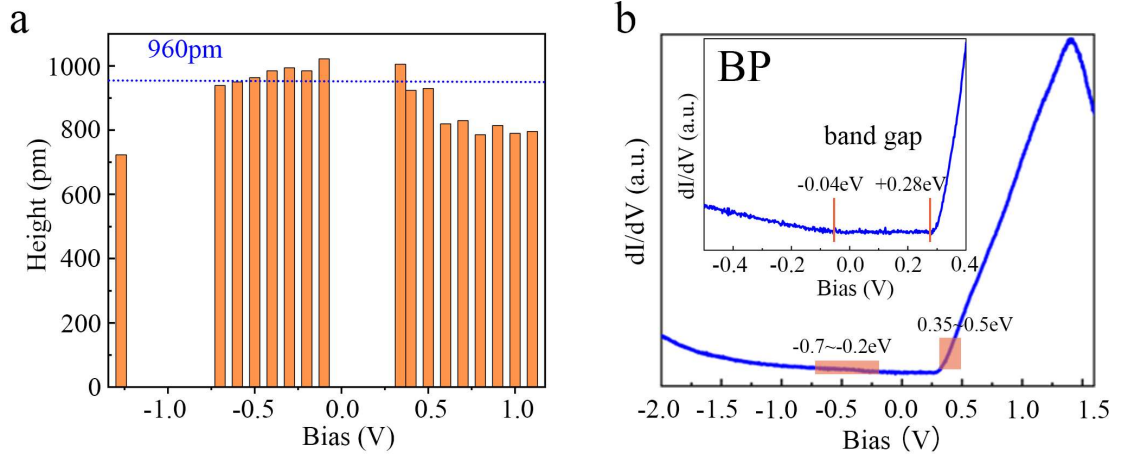
Two-dimensional Dirac nodal-line semimetal against strong spin-orbit coupling in real materials

Extended Data Figure 1



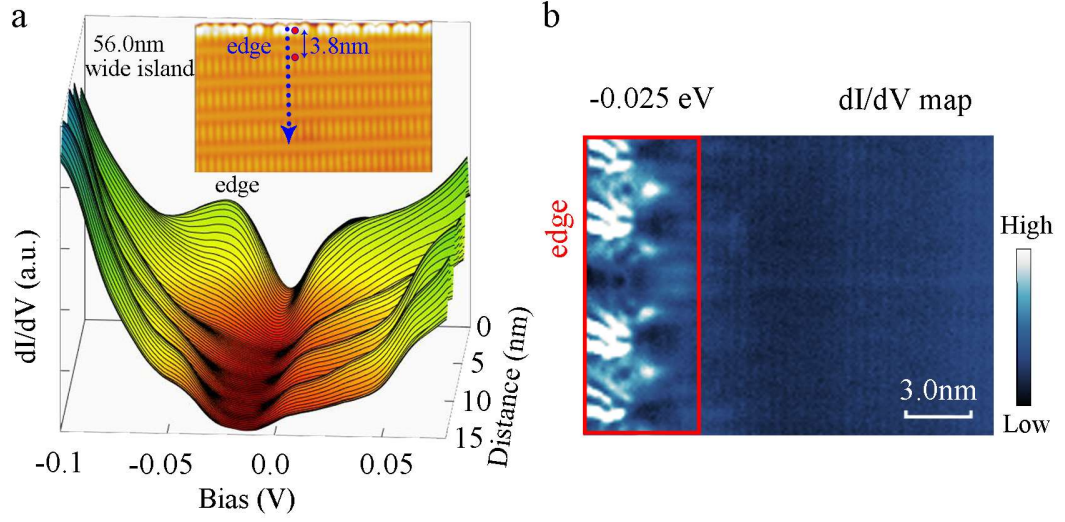
Extended Fig. 1 STM topographic images of Bi islands grown on BP surface. **a**, Large scale STM image showing that the islands grow with a preferred azimuth along the zigzag direction of the substrate. **b**, High resolution STM topographic height image showing the atomic contrast in Bi island and in BP substrate. **c**, Current image of (b) showing the zigzag chains inside Bi island and in BP substrate. Because of the big height difference, the atomic feature of both the Bi island the BP substrate is more clearly resolved by the topographic current image. It is clear that the BP zigzag chains and Bi zigzag chains are oriented almost in parallel. All the images are obtained at LN₂ temperature.

Extended Data Figure 2



Extended Fig. 2 STM measured height of Bi islands on BP surface under different biases. **a**, The height of the Bi islands varies upon different bias and centers at ~ 960 pm in the bias range from -0.7 eV to -0.2 eV and 0.35 eV to 0.5 eV . We suggest this is because at the bias away from these energy ranges, the BP substrate is characterized with a higher density of state (DOS), as shown in **b**. This makes the STM measured height of Bi islands on BP smaller than the real value. This phenomenon is more obvious at positive voltages, where the BP substrate hosts a very high DOS in the conduction band (Guo et al., Linear Scanning Tunneling Spectroscopy Over A Large Energy Range in Black Phosphorus, J. Appl. Phys. 124, 045301 (2018)). To exclude the influence of the DOS from BP substrate, we conclude that the measured height under the bias around the band gap edges is close to the real value. The measured average 960 pm height in this energy range is consistent with three atomic layer height of Bi (110) structure.

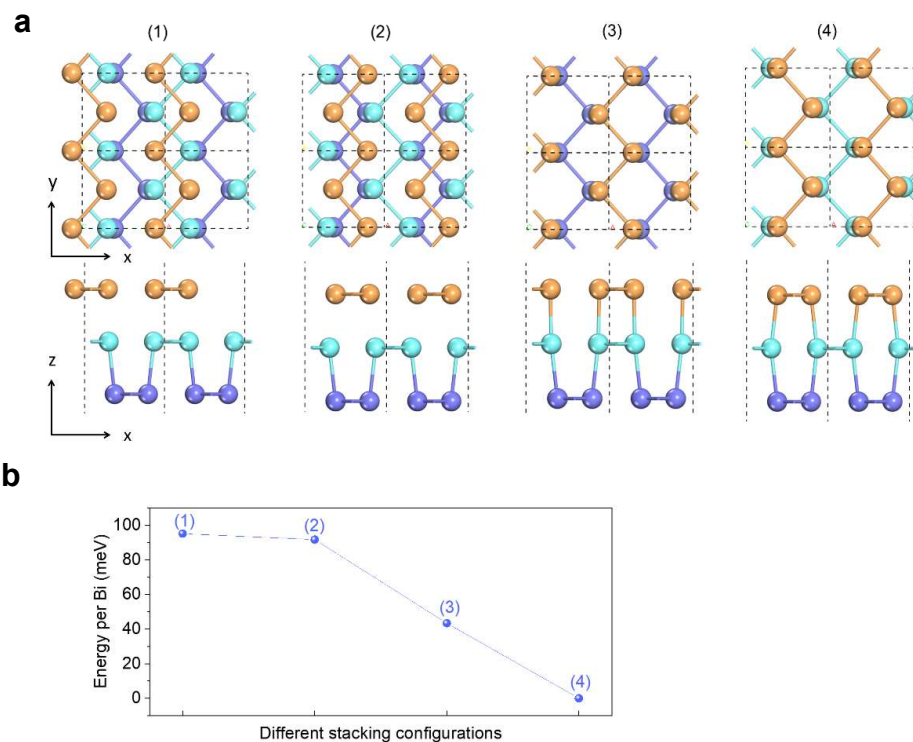
Extended Data Figure 3



Extended Data Fig. 3 Topological edge states of 3-ALs Bi (110) 8x10 superlattice.

a, Series STS dI/dV spectra measured along a line normal to the edge. The island has a width of 56 nm. The islands show an edge state at -0.025 eV, which is at the same energy value from 33 nm wide island in Fig. 1e. The edge state penetrates into the island for ~ 3.8 nm, similar as that observed in Fig. 1e. **b**, dI/dV mapping acquired at -0.025 eV. The bright contrast at edge denotes the real space location of the edge state. We notice that there is an uneven contrast brightness from the edge state. This unevenness might result from the fact of partly irregular atomic organization at edges and the hybridization of edge state with substrate (Drozdov et al., One-dimensional topological edge states of bismuth bilayers, Nat. Phys. 10, 664-669 (2014)). The robustness and reproducibility of the measured edge state in islands with different sizes eliminate the possibility of quantum confinement effect induced additional electronic peaks in the spectra.

Extended Data Figure 4



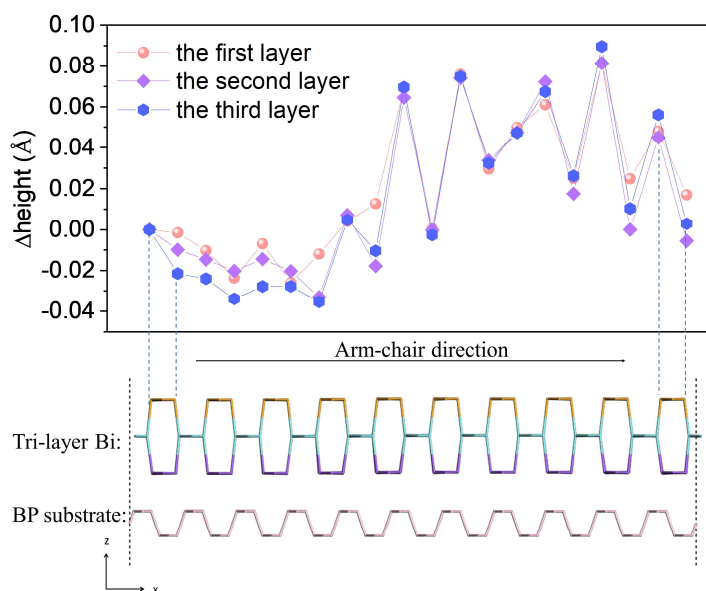
Extend Data Fig. 4 Different stacking configurations and energies for 3-ALs Bi. **a**, Four different stacking configurations (1-4) considered in 3-ML Bi (atoms in different layers are presented in different colors). **b**, Energy per Bi atom of the four different stacking configurations in 3-ALs Bi. It can be seen that the energy of configuration (4) is about 40 meV per Bi atom lower than that of configuration (3), showing that configuration (4) is the most stable configuration.

Extended Data Table 1

Freestanding		On substrate (BP)			
Layers	E_{total} (meV/Bi atom)	Layers	$E_{\text{Adsorption}}$ (meV/Bi atom)	Layers	E_1 (meV/Bi atom)
2 AL	-3939.2	2 AL	-78.9	2 AL	-4018.1
3 AL	-3984.1	3 AL	-102.0	3 AL	-4086.1
4 AL	-4043.3	4 AL	-46.6	4 AL	-4089.9
(2AL+4AL)/2	-3991.2	(2AL+4AL)/2	-62.75	(2AL+4AL)/2	-4054.0
$\Delta E_{\text{total}} = -7.2$		$\Delta E_{\text{adsorption}} = 46.6$		$\Delta E_1 = 32.1$	

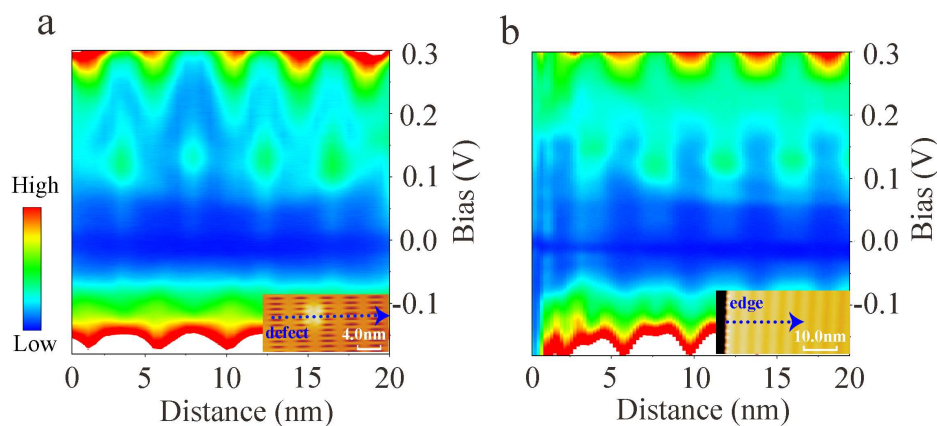
Extended Data Table 1 Total energy of different Bi atom layers and the adsorption energy on BP substrate. E_{total} represents total energy of freestanding Bi atom layers. $E_{\text{Adsorption}} = (E_{\text{total1}} - N_{\text{Bi}} \cdot E_{\text{Bi}} - N_{\text{P}} \cdot E_{\text{P}}) / N_{\text{Bi}}$, where $E_{\text{Adsorption}}$ is the adsorption energy of Bi atom layers on BP substrate, E_{total1} is the total energy of the system, N_{Bi} , N_{P} , E_{Bi} , E_{P} represent the number of Bi atoms and P atoms, the energy of single freestanding Bi atom and P atom, respectively. $E_1 = E_{\text{total}} + E_{\text{Adsorption}}$, $\Delta E = (E_{2\text{AL}} + E_{4\text{AL}}) / 2 - E_{3\text{AL}}$. Without BP substrate, the total energy of bilayer, tri-layer and four monolayer Bi is -3939.2 , -3984.1 and -3991.2 meV/Bi atom, respectively. Comparing the total energy of the (2 AL+4 AL)/2 and 3 AL Bi, it is found that the former energy is 7.2 meV/Bi lower. This indicates that 3 ML Bi is less stable than (2 AL+4 AL)/2 Bi without substrate. On BP substrate, the adsorption energy of bilayer, tri-layer and four monolayer Bi is -78.9 , -102 and -62.75 meV/Bi, respectively. The adsorption energy of 3 AL Bi is higher than those of 2 AL and 4 AL Bi, and the difference between (2 AL+4 AL)/2 and 3 ML Bi is 46.6 meV/Bi. The E_1 of 3 ML Bi is -4086.1 meV/Bi as the result of adsorption energy of 3 AL Bi on the BP substrate is the largest, and it is 68 and 32.1 meV/Bi lower than 2 AL Bi and (2 AL+4 AL)/2 Bi, respectively. This suggests that the 3-AL Bi structure is more stable than 2-AL Bi when adsorbed on BP substrate.

Extended Data Figure 5



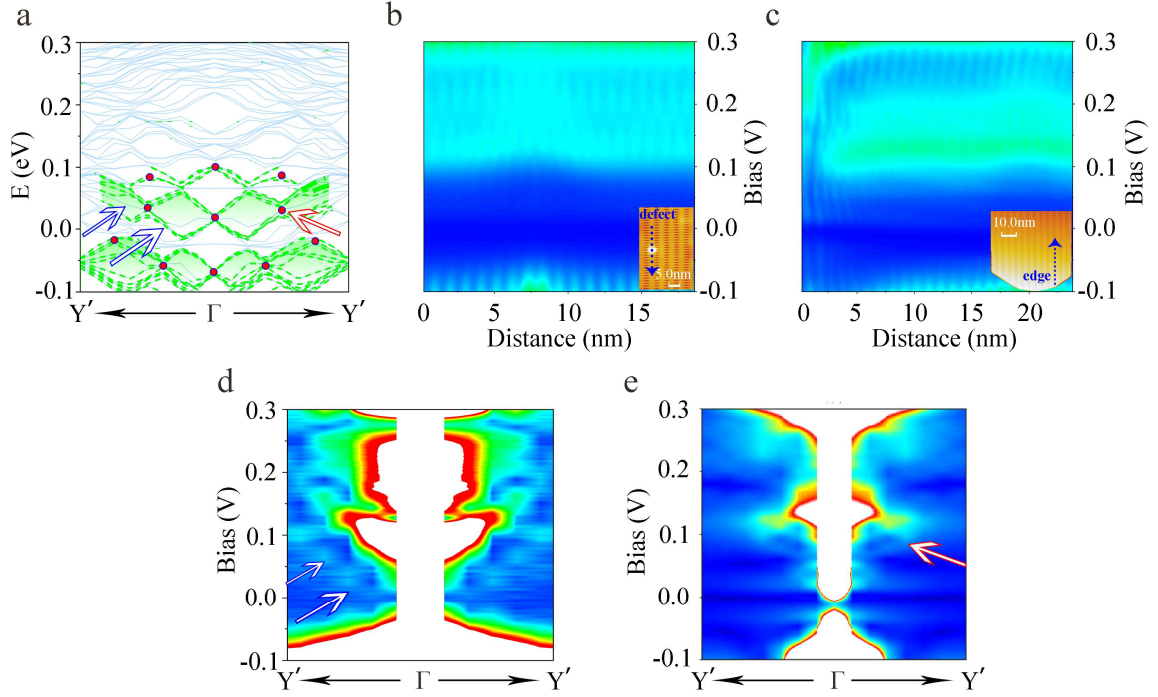
Extended Data Fig. 5 Height variation of Bi atoms in different layers of the 3-ALs Bi in a row of atoms ($10 \times L_{ac}$) along the AC direction. It shows that the heights of some Bi atoms decrease, while others increase, but the height variation of Bi atoms in different layers features the similar tendency. This indicates that the Bi atoms in three layers follow exactly the same real space trajectory.

Extended Data Figure 6



Extended Data Fig. 6 2D dI/dV spectrum map of series dI/dV spectra along AC direction. a, b 2D dI/dV spectrum map of series dI/dV spectra acquired on a line along ZZ direction, by crossing a typical defect on surface (a) and from the edge (b) of the island. The insets in both images show the locations where the spectra are acquired. One can see the QPI features when closing to the defect and edge.

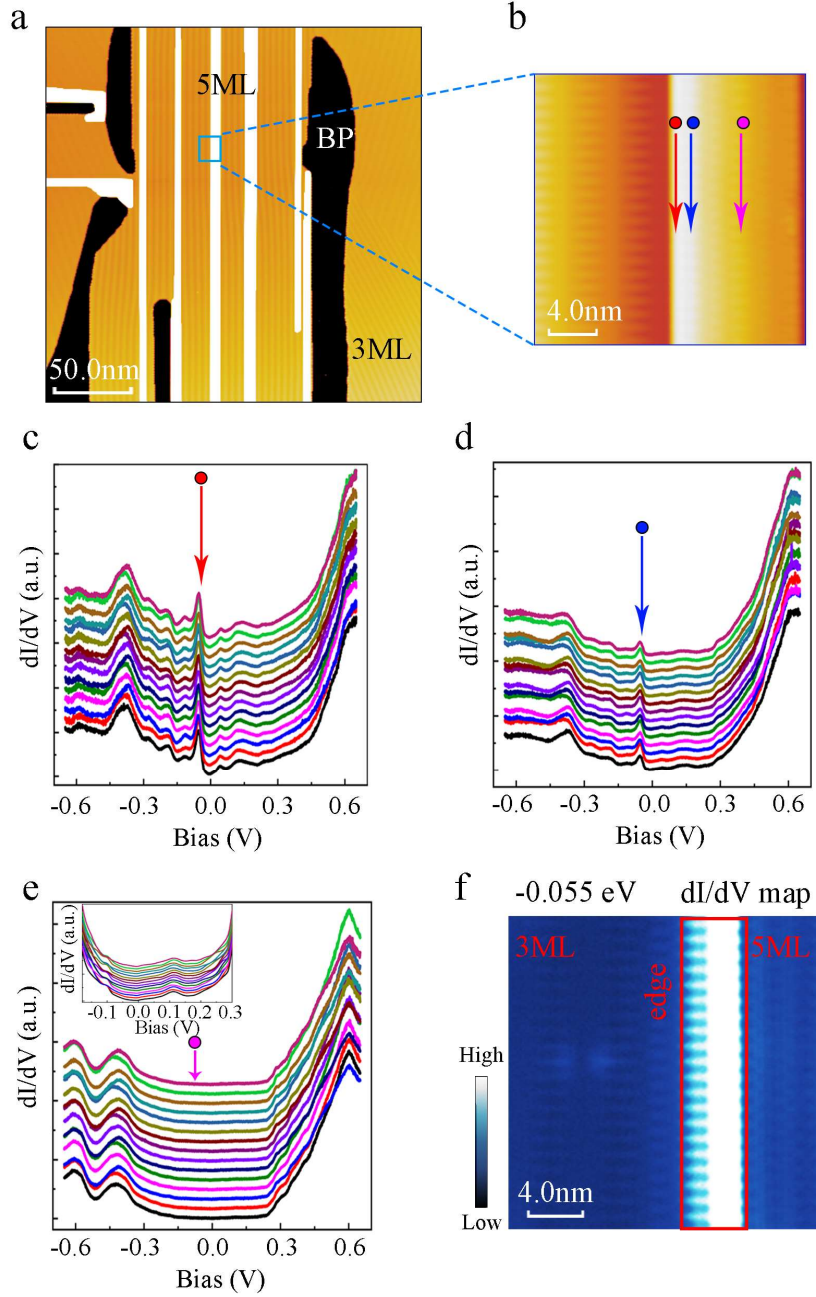
Extended Data Figure 7



Extended Data Fig. 7 Band E-q dispersions of 3-ALs Bi (110) on BP surface along $Y'-\Gamma-Y'$ direction. **a**, Calculated band structures along $Y'-\Gamma-Y'$ direction for Bi (110) 8×10 superlattice on BP. The 1st BZ of the superlattice is shown as the inner red rectangle in Fig. 1c. The green color highlights the bowtie-shaped rhombuses in the band structure along $Y'-\Gamma-Y'$, which is caused the folded linear bands from X-M to $\Gamma-Y'$. The red dots highlight the folded Dirac cones at Y point. **b**, **c**, 2D dI/dV spectrum map of series dI/dV spectra acquired on a line along ZZ direction, by crossing a typical defect on surface (b) and from the edge (c) of the island. The insets in both images show the locations where the spectra are acquired. One can see the spectrum changes caused by QPI when closing to the defect and edge. **d**, **e**, E-q dispersions along $Y'-\Gamma-Y'$ obtained from QPI scattering by surface defect (d) or by the edge (e) by performing FFT on the corresponding series dI/dV spectra. Several bow-tie shapes (marked by the blue-white arrows), originating from the crossing of the linear bands, are seen in (d). Because of the strong scattering at the edge, the QPI pattern is relatively sharp in (e).

and a clear Dirac point appears in the QPI as marked by the red-white arrow. The colored arrows help to point out the resolved q as those marked in (a).

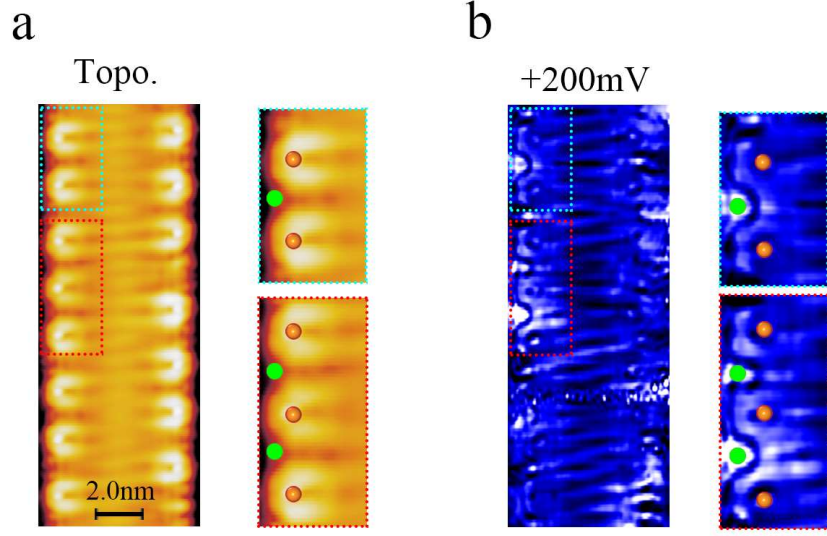
Extended Data Figure 8



Extended Data Fig. 8 Topographic STM images of 5-ALs Bi nanoribbons grown on BP substrates and the topological edge states measured by STS dI/dV spectra. **a**, STM image shows the coexistence of 3-ALs Bi and 5-ALs Bi on BP substrate. When continually increasing the Bi atom deposition, 3-ALs Bi will form large area continuous thin films. Then 5-ALs Bi structures are obtained with two additional atomic Bi layer grown on top of the 3-ALs Bi. **b**, The zoom in STM image shows the edge

at the 3-ALs and 5-ALs Bi interface. The 5-ML Bi shows similar STM contrast as those in 3-ALs Bi. **c to e**, The series STS dI/dV spectra measured along the red, blue and pink arrows in (b). In (c), the data shows an obvious edge state at -0.055 eV. When moving slightly away from the edge to the center as shown in (d), the edge state peak becomes gradually weaken. When far away from the edge as shown in (e), the edge state totally disappears. The inset in (f) shows STS spectrum at small energy range, indicating very similar electronic characters of 5-ALs Bi with that of the 3-ALs Bi. **f**, The dI/dV mapping acquired at -0.055 eV clearly shows the space distribution of edge state of a 5-ALs Bi island. The edge of 5-ALs Bi is much more ordered than that of 3-ALs Bi, and there is no hybridization with BP substrate. These make the edge state mapping possesses a uniform contrast. The edge state penetrates into the island for ~ 4.0 nm.

Extended Data Figure 9



Extended Fig. 9 STM topographic and mapping images of narrow Bi islands grown on BP surface. a, STM topography image showing that the island does not have the corrugation along AC direction, as a result of the narrow width of the island. At the edge of the island, STM image shows continuous “s”- shaped contrast. **b,** STM dI/dV mapping image highlights the DOS at the edges. The orange and green balls are markers to show two kinds of edge defects locations. It could be seen that the DOS escape perfectly from the defects to form “s”-shaped distributions at the edges, indicating that electronic state could pass the defects smoothly. This S -like 1D electronic state is typical at the energy within the DNL energy window and is subject to future investigations.